In Situ Operando Investigations of the Thermal Instability Mechanisms of a Deformed Ti-48Al Alloy

P.S Sankara Rama Krishnan, Joseph V Vas, Soumya Ranjan Mishra, Xuesong Xu, Karl Peter Davidson, Shakti P. Padhy, Martial Duchamp, R. V Ramanujan

Abstract

TiAl based alloys are currently deployed in extreme service environments, such as jet engine turbine blades. The microstructure of these alloys is a two-phase lamellar structure, comprising of the majority γ-TiAl and the minority α_2-Ti_3Al phases. Understanding the microstructural evolution at high stresses and elevated temperatures is a key requirement to develop the next generation of these alloys. In situ hot stage TEM studies are reported of the mechanisms of lamellar instability and changes in phase fraction of both cold worked and undeformed Ti-48Al alloys. The effect of cold working on the kinetics of this instability has also been determined. Cross-sectional TEM samples are prepared on custom designed MEMS chips and in situ heating studies carried out. These results show that neck formation, break-up of lamellae, and spheroidization are the dominant mechanisms of microstructural instability. An increase in γ-TiAl phase content is also observed. The strain energy present in the α_2 and γ lamellae in cold worked samples results in microstructural instabilities occurring at lower temperatures in cold worked samples. These findings can be used to design new alloys with improved high temperature stability.

1 Introduction

In the regime of materials for extreme environments, TiAl based alloys are of significant interest as they exhibit superior high temperature mechanical properties. These alloys are widely used in aerospace[1-4] and automobile components,[5, 6] such as low pressure turbine blades in aircraft jet engines[7] and turbochargers in passenger vehicles.[5, 8] The key features of TiAl alloys which makes them suitable for such structural applications are their high strength to weight ratio, low density, and good temperature oxidation and corrosion resistance.[9-11]

To improve the service temperature and lifetime of TiAl based alloys, it is necessary to have excellent microstructural stability of these alloys at high temperatures. Although various thermal treatments can result in equiaxed grains or duplex structures, the most common and desirable microstructure of these TiAl based alloys consists of a two phase lamellar structure, comprising of parallel plates of the γ-TiAl (tetragonal) and α_2-Ti_3Al (hexagonal) phases, as well as a small volume fraction of equiaxed γ grains.[12-14]

Temperature and stress can induce instability of the lamellar structure, leading to severe degradation of the material during service and consequent decreases in mechanical properties.[15, 16] Continuous and discontinuous coarsening of the lamellae, branching, neck formation and dissolution at regions with a high defect density, migration of existing dislocations, changes in the interlamellar spacing, and spheroidization are typical instability mechanisms.[17, 18] These driving force for these instabilities can be a reduction in chemical free energy or interfacial energy, or elastic strain energy.

Previous research has examined such instabilities for various TiAl based compositions, processing routes and a range of temperatures.[19-23] These investigations of the instability mechanisms were typically *postmortem* investigations performed at room temperature, after subjecting the alloys to high temperature heat treatment, hence they do not provide direct insight into the instabilities occurring at elevated temperatures. Hsiung et al. performed in situ straining experiments at room temperature and concluded that the cooperative movement of interfacial dislocations at lamellar

interfaces can lead to lamellar instability.[24] Recently, Liu et al. used synchrotron based in situ high energy X-ray diffraction to study the strain evolution at high temperatures.[25] *To rationally design the next generation of TiAl based alloys with better microstructural stability, we deploy an* in situ *TEM based technique with superior spatial resolution to observe the origin of these instabilities at high temperatures (800-900 °C)*. This approach provided insight and a broad understanding of the origin and evolution of lamellar instabilities at elevated temperatures.[26, 27]

Recent developments in in situ and operando techniques in transmission electron microscopy (TEM) make them ideal for studying the microstructure with high spatial resolution.[28-31] TEM can also provide other relevant information such as microstructural changes, local phase transitions, and changes in chemical composition in response to in situ stimuli.[32, 33] The present study utilities these capabilities to study microstructural changes in TiAl based alloys at elevated temperatures. As a comparison, we have also conducted ex situ heat treatments and subsequently conducted microstructural investigations. We find that a key lamellar instability mechanism is initiation of instability by neck formation, followed by lamellar breakup and spheroidization of α_2- lamellae.

2 Experimental Section

Figure 1a is the schematic experimental procedure for sample production and characterization. An alloy with the Ti-48Al (atomic%) composition was prepared from Ti (99%, Alfa Aesar) and Al (99.5%, Alfa Aesar) powders. The powders were consolidated and cast into buttons using an arc melter. From the buttons, cylinders of 3 mm diameter × 4.5 mm length were fabricated. The phase analysis was conducted using a X-ray diffraction (XRD) Bruker D2 phaser equipment in θ-2θ mode with a CuKα radiation source and wavelength (λ) of 0.154 nm. A step size of 0.02 degrees and time per step of 80 s was employed for all the measurements. Semi-cylindrical samples with 2 mm × 3 mm cross sectional surface area were used for XRD measurements. In order to address preferential orientation observed in arc melted samples, the samples were rotated at 15 RPM using a spinner stage in the XRD. Rietveld refinement of the obtained XRD patterns was carried out using X-Pert highscore plus. The XRD profiles were fitted using a Pseudo-Voight function. The poor goodness of fit from Rietveld refinement is owing to the preferred orientation of the arc melted and strained samples. The data given in Table **S1** (Supporting Information) is only meant for qualitative comparison. Some of the samples were compressed at room temperature to 5.35% strain using an Instron 580 UTM equipment. This prestrain can contribute significantly to lamellar instability at elevated temperatures.

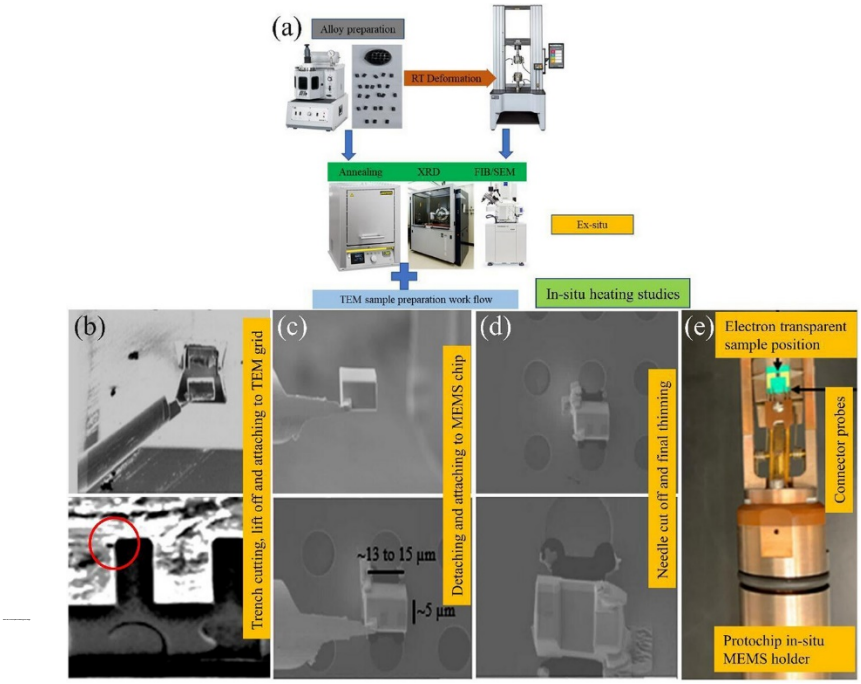

Figure 1

Open in figure viewerPowerPoint

(a) Schematic of the process flow of in situ operando TEM experiments, (b–d) FIB-SEM images showing the in situ TEM sample preparation work flow starting form trench cutting to attaching to the MEMS chip. The red circle highlights the attachment of sample to TEM grid prior to transfer to MEMS chip (e) The sample attached to a MEMS chip and then placed in the custom-built Protochip in situ TEM holder for in situ heating experiments.

Studies were performed on deformed and undeformed samples, henceforth called room temperature deformed-TiAl (RTD-TiAl) and non-room temperature deformed (NRTD-TiAl), respectively. Both the deformed and the undeformed samples were subjected to heat treatment in a laboratory furnace for the ex situ instability mechanism studies. RTD and NRTD TiAl samples were vacuum sealed in quartz tubes and annealed in a furnace for 1 hr at either 750 and 820 °C.

Cross-sectional electron transparent samples were prepared using a Carl Zeiss Crossbeam 540 focussed ion beam (FIB), as shown in Figure 1b. The protocol followed was similar to those reported by Tyukalova et al.[34] The sample was transferred to a commercial MEMS chip procured from Protochips, USA. To minimize surface strains, 2 min exposure of the MEMS chips in a hydrophobic chamber (JEOL, Japan) was performed. In the MEMS in situ specimen chip design, the electron transparent specimen is placed across an electron transparent silicon nitride window attached to electrical contacts, enabling in situ heating.[35, 36] The sample was attached on only one side to accommodate expansion during in situ heating. The MEMS chip with the electron transparent sample is loaded in a Protochips Audro in situ heating holder for TEM studies (Figure 1c). This MEMS chips along with the Protochips Audro holder assembly was designed such that uniform heat distribution is feasible at higher temperatures, enabling a greater control on the temperature profile irrespective of the thickness of the sample. High temperatures (room temperature to 1200 °C) and a range of heating rates (5–250 °C min^{-1}) can be produced by Keithley source meter controls.

In situ TEM experiments were carried out in a double corrected JEOL ARM300F operated at 300 kV. The scanning transmission electron microscopy (STEM) mode was used, specifically with a high angle

annular diffraction (STEM-HAADF) technique with a probe size of 10–20 pm and a collection angle of 220–250 mrad. In STEM-HADDF images, the contrast is directly related to the atomic number (Z^n) of the elements present in the sample.[37-40] Before starting the heating cycle, in the STEM-HAADF mode, using Ronchigram, the samples were aligned in (101) zone axis with respect to the beam. Heating was achieved using a Keithley source control at a heating rate of 100 °C min^{-1} up to 700 °C and 5 °C min^{-1} up to 860 °C. Samples were held for up to a maximum of 60 min at defined intervals of 20, 30, 40, and 60 min, at temperatures of 750, 800, 820, or 840 °C, as presented in the time-temperature graph **Figure 2**. Each of the heating experiments was performed with the sample completing a thermal treatment cycle and, they were not reused in the other experiments. STEM-HAADF imaging was conducted at a range of magnifications (25, 60, 150, and 300 Kx) presented in Figure S1 (Supporting Information), selected to ensure a statistical representation of microstructural changes of the lamellae with >2 lamellar colonies present in the images. The fraction of α_2-Ti_3Al and γ-TiAl phases in the samples across all of the test temperatures and times was determined by binarizing TEM images using ImageJ software and calculating the ratio of black and white pixels. A minimum of four images were taken for each experimental condition. Interlamellar/interphase strain was mapped from TEM data using Strain++ software.

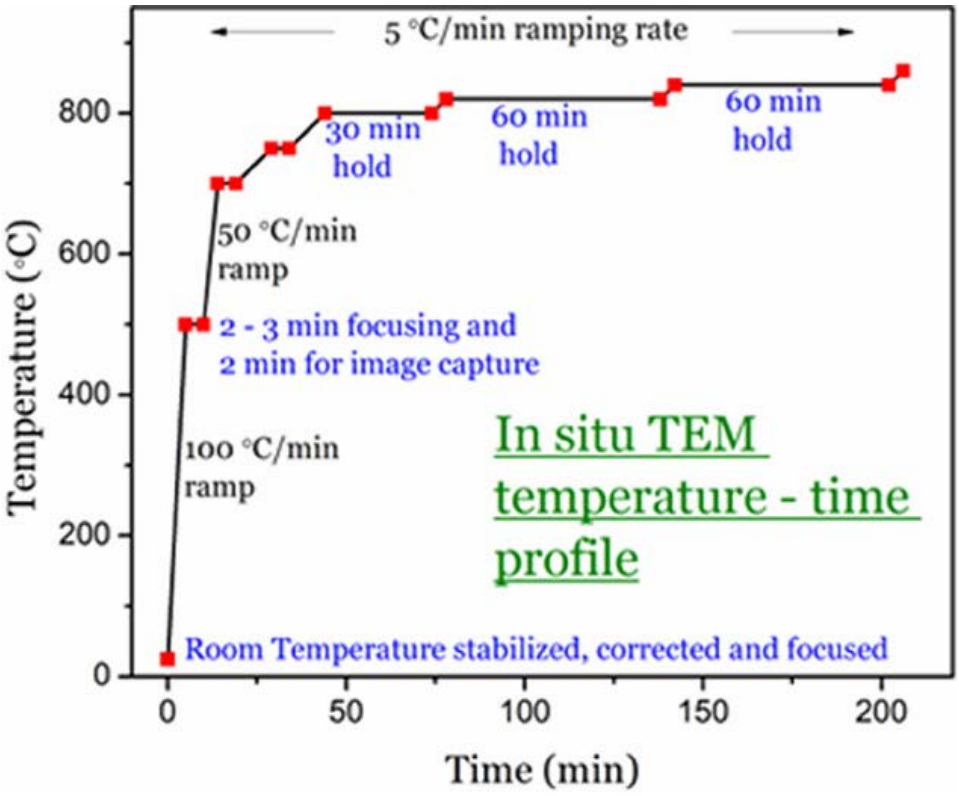

Figure 2

Open in figure viewerPowerPoint

Time-temperature profile employed in the in situ TEM experiments.

A JEOL 7800F Prime field emission scanning electron microscope was used to obtain the backscattered electron images of the microstructure. Electron backscattered diffraction (EBSD) maps are collected using an accelerating voltage of 20 kV, probe current of 30 nA, and step size of 0.15 µm by an Oxford Instruments Symmetry S2 detector and analyzed on AZtecCrystal software.

3 Results and Discussion

3.1 As Cast Microstructure

The underlying microstructure of the NRTD sample is presented below in **Figure** 3. Clear presence of the lamellar α_2-Ti_3Al and γ-TiAl structure is evident in the contrast differences of the backscattered SEM images and the phase maps Figure 3a,b. The grain orientation map in Figure 3c and γ-TiAl pole figure of Figure 3d highlights the preferred <002> orientation of the γ-TiAl phase and less orientated α_2-Ti_3Al phase.

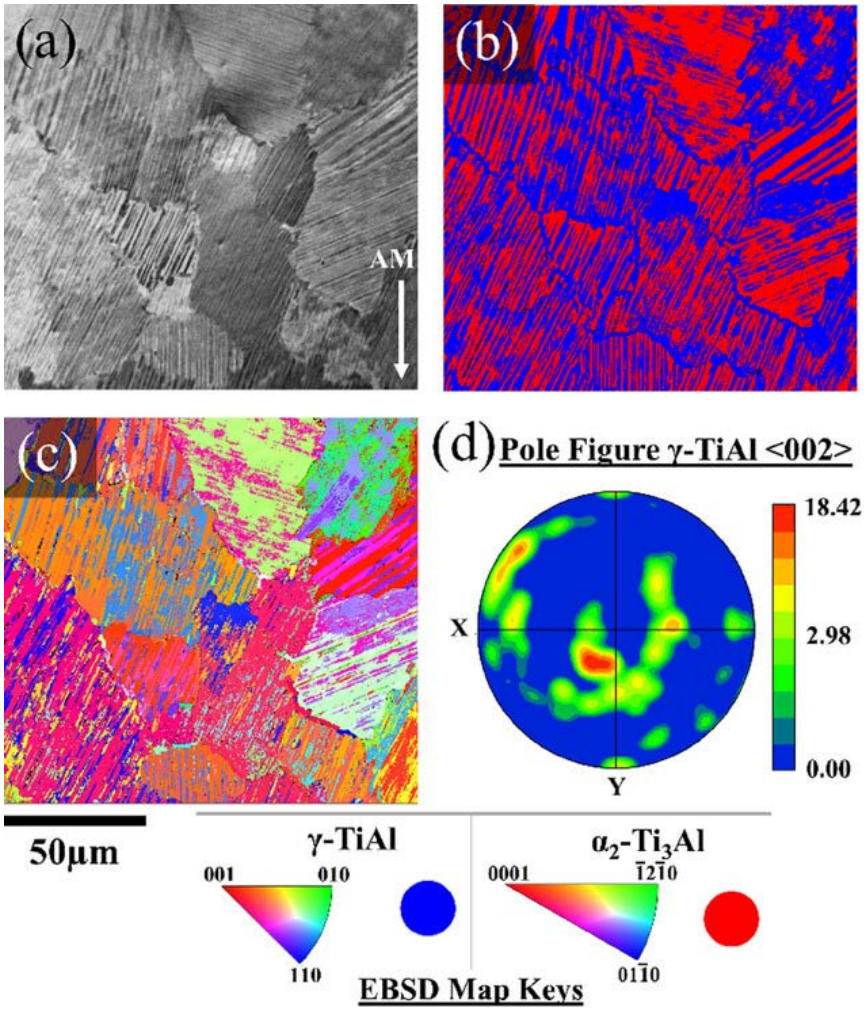

Figure 3

Open in figure viewerPowerPoint

(a) SEM image of the NRTD Ti48Al microstructure, (b) phase map, (c) grain orientation map (out-of-plane), and (d) pole figure for γ-TiAl phase at <002> orientation and EBSD map keys. Arrow denotes arc melting (AM) direction.

3.2 In Situ TEM Studies of RTD and NRTD Ti48Al Alloys

The XRD results of the RTD and NRTD Ti-48Al samples are shown in **Figure** 4a, which confirm the presence of the α_2-Ti_3Al and the γ-TiAl phases in both samples. The α_2-Ti_3Al phase exhibits *P 63/mmc* symmetry (hexagonal), the γ-TiAl phase has a P 4/mmm symmetry (tetragonal). In the NRTD samples, a slight preferred orientation is observed in the <002> direction for γ-TiAl phase as seen in Figure 3d. Also evident is the preferential orientation (<021>) of the α_2-Ti_3Al phase in the RTD sample (near 2θ of 41°), indicative of the direction of the applied strain (deformation) in the RTD samples, as similarly observed in other TiAl intermetallic alloys.[41] Hence, it can be stated that due to the room temperature deformation, a preferred orientation could be observed in the (021) plane of the α_2-Ti_3Al

phase.

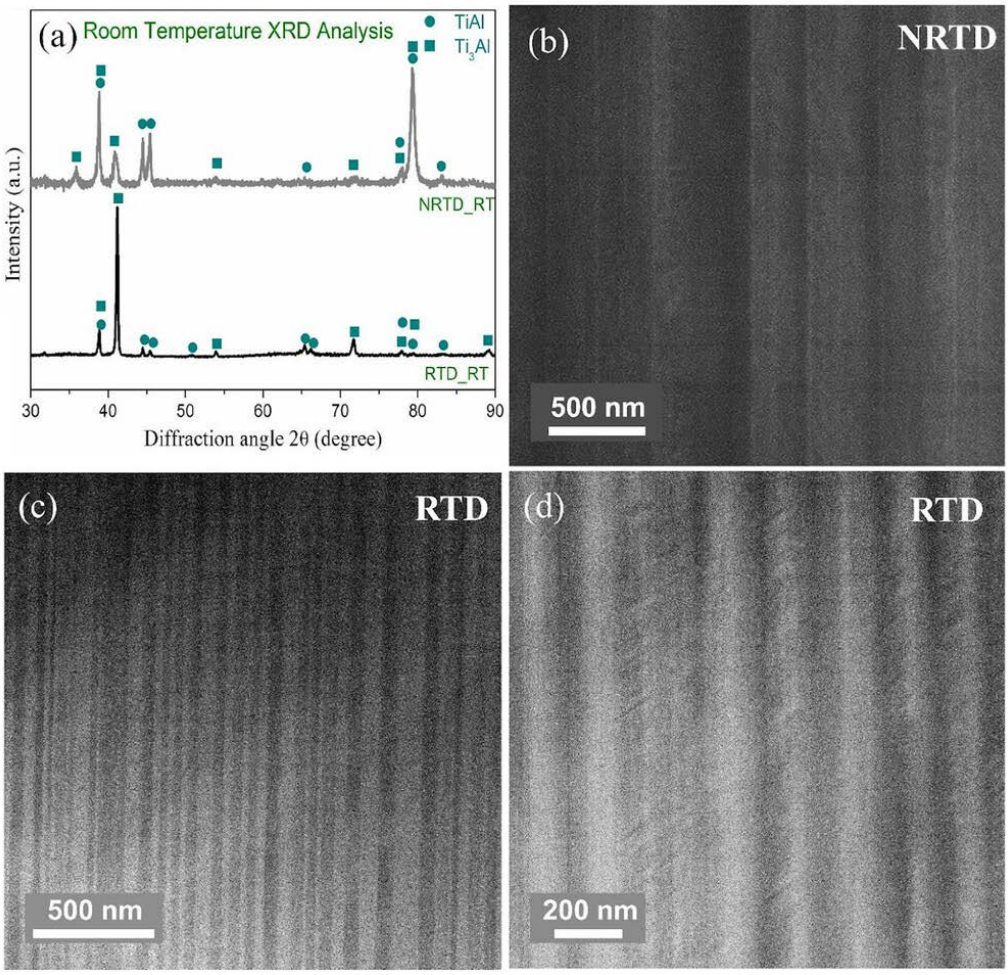

Figure 4

Open in figure viewerPowerPoint

(a) XRD of the room temperature deformed (RTD) and non-room temperature deformed (NRTD) Ti48Al alloy, (b) STEM-HAADF images of the NRTD, and (c) RTD samples, (d) high magnification image of the RTD sample.

The STEM-HAADF images show a well-defined contrast, consistent with the two-phase lamellar structure of TiAl and Ti_3Al in both the NRTD (Figure 4b) and RTD samples (Figure 4c,d), respectively. The applied strain in the RTD sample leads to more uniformity in the lamellar spacing as compared to the NRTD sample leading to a decrease in average lamellar spacing from 154 ± 23 nm in the NRTD sample to 95 ± 4 nm in the RTD sample (Figure 4b,c).

3.2.1 RTD-TiAl Samples

The evolution of instability as a function of temperature and time was studied using in situ TEM experiments. STEM-HAADF images of in situ heated RTD and NRTD TiAl samples on the MEMS chip is shown in **Figure** 5a, for temperatures ranging from room temperature (RT) to 840 °C. The white dotted box in Figure 5a-V represents the reference lamellar location over which the instability mechanism is followed and observed as the change in temperature induces a thermal shift and slight changes in the imaging position. The STEM-HAADF contrast arises from the bright α_2-Ti_3Al phase, and the dark contrast are from the γ-TiAl phase, due to the difference in the Ti content of these two phases. There are no significant changes in the lamellar stability until 700 °C. At 750 °C, the α_2-Ti_3Al lamellae start

to show neck formation, as indicated by the white arrow in Figure 5a-V.

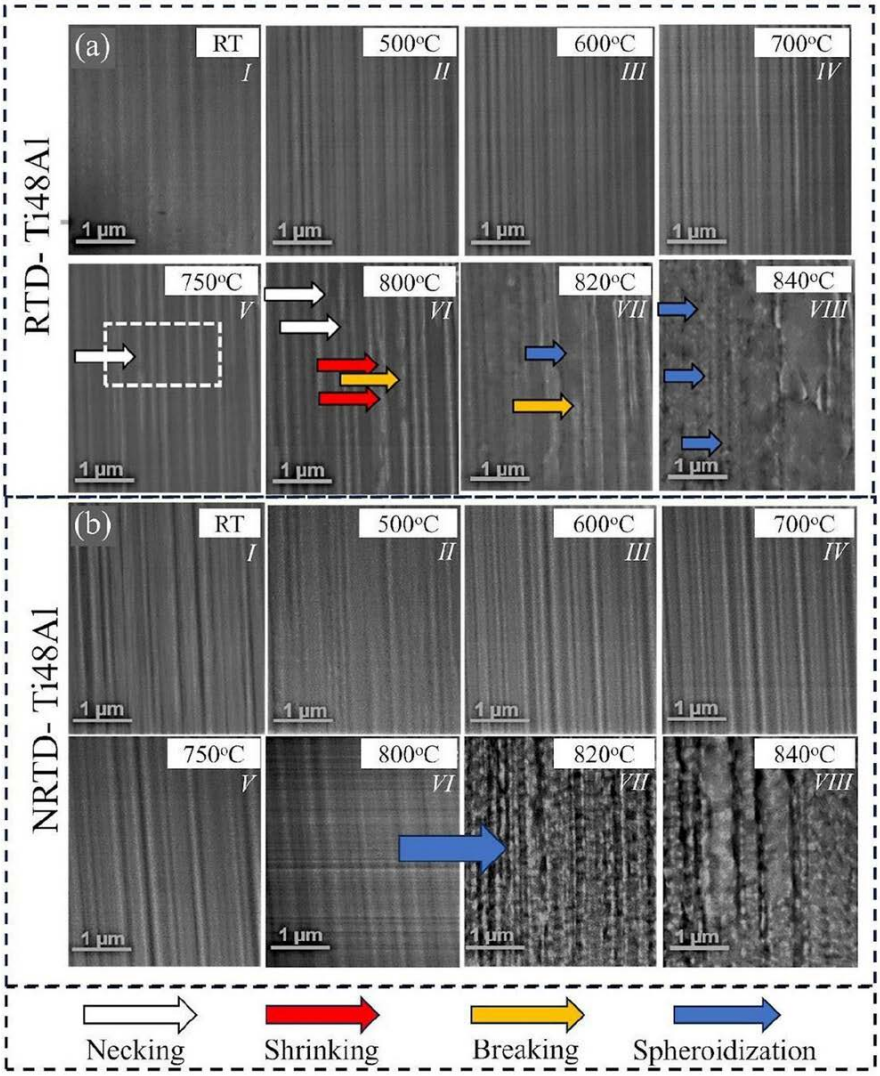

Figure 5

Open in figure viewerPowerPoint

(a) In situ STEM-HAADF images of RTD Ti48Al samples, (b) In situ STEM-HAADF of NRTD samples.

At 800 °C, Figure 5a-VI, a greater number of α_2-Ti_3Al lamellae start to form necks, as indicated by multiple-white arrows. Further shrinking of the lamella neck region (red arrow) and breakup of the lamellae into smaller segments (yellow arrow) along the lamellar direction takes place. At this temperature, multiple instability mechanisms come into play to destabilize the α_2-Ti_3Al lamellae. The regions of dark contrast (γ-TiAl phase) also start to increase significantly, indicating an α_2-γ phase transformation.

Increasing the temperature to 820 °C, as shown in Figure 5a-VII, leads to further breakup of the α_2-Ti_3Al lamellae and spheroidization (blue arrow) takes place. When the temperature reaches 840 °C (see Figure 5a-VIII), the instability of the original lamellar structure is complete. The two-phase lamellar microstructure has transformed to a globular microstructure, consisting mainly of the gamma phase.

In summary, the transformation follows the following sequence: a) the formation of necks in the α_2-Ti_3Al phase, b) shrinkage of necks, c) breakup of α_2-Ti_3Al lamellae into segments and d)

spheroidization.

3.2.2 NRTD-TiAl Samples

The STEM-HAADF image of the NRTD-TiAl sample (Figure 5b), for temperatures ranging from room temperature (RT) to 840 °C, showed no significant changes in the lamellar structure until 800 °C. At 820 °C, as shown in Figure 5b-VII, the α_2-Ti_3Al lamella undergo necking and *quick spheroidization*. On further increase of the temperature to 840 °C (see Figure 5b-VIII), the lamellar structure transforms completely to globular. *In NRTD samples instability takes place sharply at 820 °C, rather than over the temperature range of 750–820 °C, as observed in the case of RTD samples, the instability is dominated by spheroidization*.

3.3 In Situ TEM Studies of RTD Ti48Al Alloy with Respect to Time

As is evident in the prior section, RTD samples show a slower, more incremental deformation path with multiple deformation steps, making it less challenging to observe with our experimental setup. Hence, we studied the influence of holding time on lamellar instability exclusively on these samples. The kinetics associated with the destabilization of the lamellar structure were also studied by in situ heating over a range of times up to 60 min.

The STEM-HAADF images are shown in **Figure** 6a with the corresponding time-temperature profile outlined in Figure 2. As observed earlier, in this case also, there are no changes in the lamellar stability till 700 °C (not shown). At 800 °C (0, 10, 20, 30 min), the images clearly show the start of necking and breakup of the α_2-Ti_3Al lamellae into small segments at random locations (Figure 6a I-IV). On reaching 820 °C (0, 10, 20, 30, 60 min) (Figure 6a V-X), breakup and spheroidization of the α_2-Ti_3Al lamella dominates. At 840 °C (0, 60 min) (Figure 6a XI-XII), complete destabilization of lamellar structure can be observed. The schematic diagram capturing the lamellar instability initiation, progression, and complete instability is shown in Figure 6b. The gif file in as represented in Figure S2 (Supporting Information) depicts these transformations that show the effect of temperature and time on a single region studied through in situ TEM.

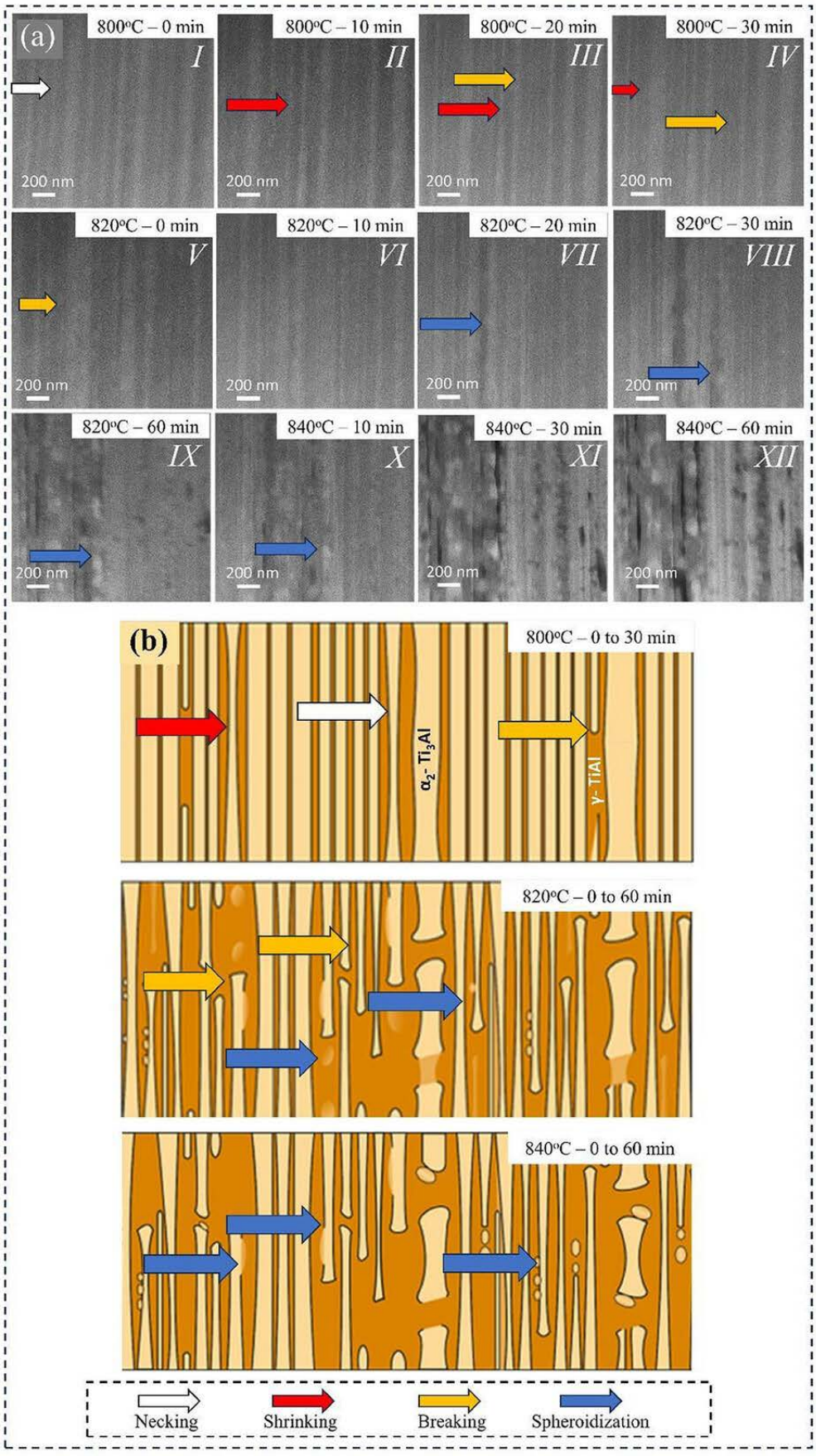
(a)
800°C – 0 min
I
800°C – 10 min
II
800°C – 20 min
III
800°C – 30 min
IV
820°C – 0 min
V
820°C – 10 min
VI
820°C – 20 min
VII
820°C – 30 min
VIII
820°C – 60 min
IX
840°C – 10 min
X
840°C – 30 min
XI
840°C – 60 min
XII
200 nm
(b)
800°C – 0 to 30 min
α2- Ti3Al
γ- TiAl
820°C – 0 to 60 min
840°C – 0 to 60 min
Necking
Shrinking
Breaking
Spheroidization

Figure 6

Open in figure viewerPowerPoint

(a) In situ STEM-HAADF images of RTD Ti48Al sample imaged at different time intervals. (b) Schematic of thermal instability destabilization mechanism in the RTD Ti48Al alloy.

3.4 Ex Situ Annealing Experiments

Figure 7a shows the XRD results for the RTD TiAl sample annealed at 750 °C for 60 min, revealing the presence of the α_2-Ti_3Al and the γ-TiAl phases, with a greater phase fraction of the α_2-Ti_3Al phase. As seen prior in the RTD samples (Figure 4a), the difference in peak heights of the NRTD and RTD samples results from the texturing effect of the alloy, whereby the applied strain in the RTD sample produces a <021> preferred orientation in the α_2-Ti_3Al phase, as observed in the samples heated up to 750 °C. This is particularly evident in the poorer goodness of fit (χ^2) parameter presented in the comparative phase analysis assessment in Table S1 (Supporting Information). This table shows the phase analysis obtained by Rietveld refinement of the XRD data. The XRD phases analysis in Table S1 (Supporting Information) reveals comparable α_2-Ti_3Al (40 wt.%) and γ-TiAl (60 wt.%) content at 750 °C. A stable lamellar structure of the RT sample is exhibited in the SEM and TEM-bright field images of Figure 7b. The TEM-BF shows contrast between the lamellae, corresponding to the two distinct phases, as verified by selected area diffraction patterns (Figure 7b-inset) confirming the crystallography of the two phases.

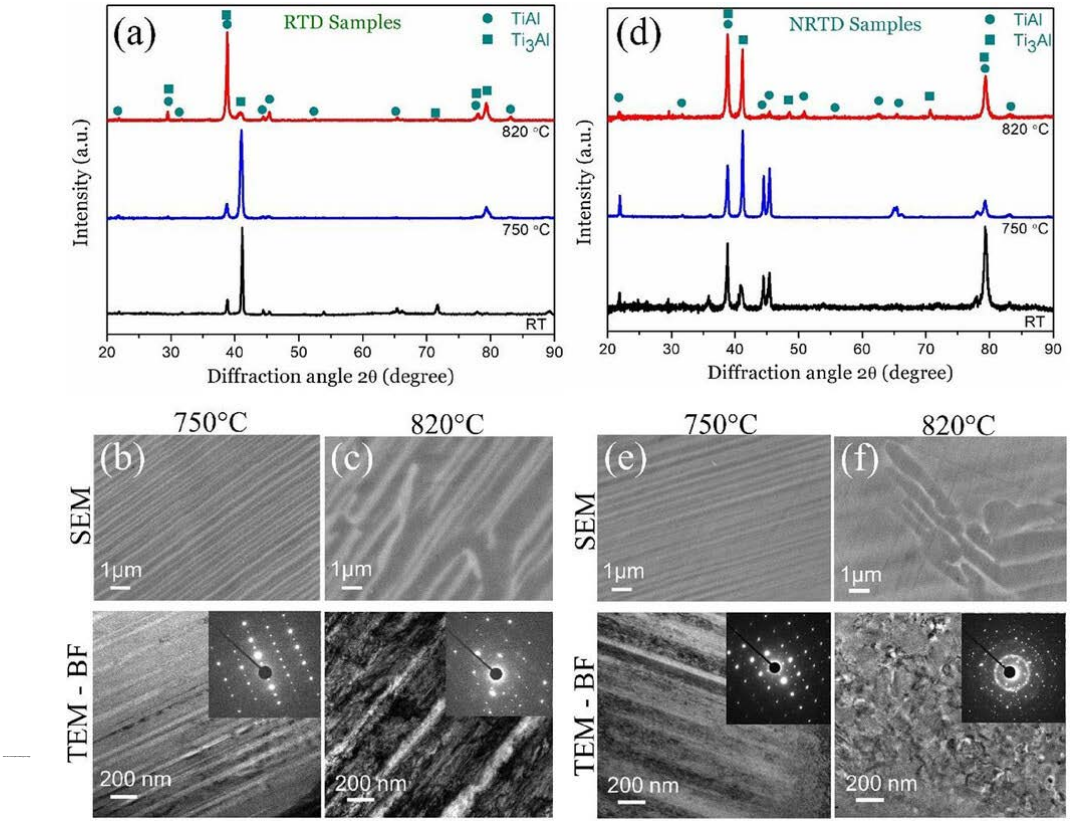

Figure 7

Open in figure viewerPowerPoint

(a) XRD of RTD Ti48Al furnace annealed at 750 and 820 °C and (b) corresponding SEM and TEM images of the annealed sample at 750 °C and (c) 820 °C respectively. (d) XRD of NRTD Ti48Al furnace annealed at 750 and 820 °C, (e) SEM and TEM images of the annealed sample at 750 °C and (f) 820 °C respectively.

The increase in γ-TiAl content of the sample heated to 820 °C for 60 min is observed in the XRD pattern

of Figure 7a, with additional γ-TiAl peaks and validated by Rietveld refinement in Table S1 (Supporting Information). The decrease in the α_2-Ti_3Al phase content is consistent with the necking, shrinking, breakup, and spherodization of the α_2-Ti_3Al phase seen in Figure 6.

SEM and TEM images confirm the complete instability of the lamellar structure by necking, shrinking, and breakup (Figure 7c). The orientation preference seen in XRD patterns of the lamellar sample (RTD-RT and RTD-750 °C) decreased when it was heated to 820 °C. This effect is evident by additional peaks corresponding to both phases, with the SAD patterns transforming from dot to ring, revealing decreased preferential orientation and increased polycrystalline character (Figure 7c).

The X-ray diffraction, TEM bright field and SEM results of the NRTD-TiAl sample heat treated at 750 and 820 °C – 60 min are shown in Figure 7d. As in the case of the RTD TiAl samples, no changes were observed in the XRD results or the SEM and TEM-bright field images (Figure 7e), which confirms no change in the lamellar stability until 750 °C. While the preferential orientation observed in the RTD samples is not as profound as observed in the NRTD samples, small texturing can be seen along the <002> direction of the γ-TiAl phase observed by EBSD (Figure 3d). At 820 °C – 60 min, the XRD results show a significant increase in the γ-TiAl content (Table S1, Supporting Information).

As observed before, the texturing effect diminishes in the RTD sample at 820 °C, with additional peaks corresponding to both the phases in the XRD pattern. The SEM and TEM images confirm the complete destabilization of the lamellar structure by spheroidization (Figure 7f), consistent with the results of the in situ TEM studies (Figure 6). The SAD insert shows a polycrystalline ring pattern, and the TEM-BF images show the loss of microstructural stability of the lamellar structure.

This two-phase lamellar microstructure with preferential orientation of the α phase at 750 °C transforms to the near γ globular microstructure at 820 °C with the particles distributed homogenously. This is clearly reflected in the SAD patterns between 750 and 820 °C (Figure 7b–f), resulting in complete instability occurring at 840 °C.

3.5 Phase Fraction and Strain Analysis

Understanding the lamellar instability of TiAl based alloys at high temperatures and stresses is very significant for the development of the next generation of high-temperature structural materials. The microstructure is unstable due to the reduction of the interfacial energy (through a reduction of the interfacial area), lower strain energy, and the tendency toward the equilibrium composition and volume fraction of the various phases. This instability can be expected to be greater in deformed samples.

Figure 8a,b provide an analysis of the phase evolution of the RTD sample with temperature and holding time, respectively, extracted from the results for the α_2-Ti_3Al and γ-TiAl phases observed in the STEM-HAADF image. The room temperature volumetric percentage is 58% and 42% for the α_2-Ti_3Al and γ-TiAl phases, respectively. This corresponds to mole percentage of 41 and 59%, respectively, which remains almost unchanged until the temperature is 600 °C. Between 750 and 800 °C, the α_2-Ti_3Al phase fraction reduces to 30.15%, while the γ-TiAl phase fraction increases to 69.85 mole%. On increasing the temperature to 820 °C, the α_2-Ti_3Al phase fraction further reduces to 28.8%, while the γ-TiAl phase fraction increases to 71.2%. Overall, there is a decrease in phase fraction of the α_2-Ti_3Al phase, with a simultaneous increase in the γ-TiAl content (Figure 8a), taking place over a temperature scale of 90 °C (750–840 °C).

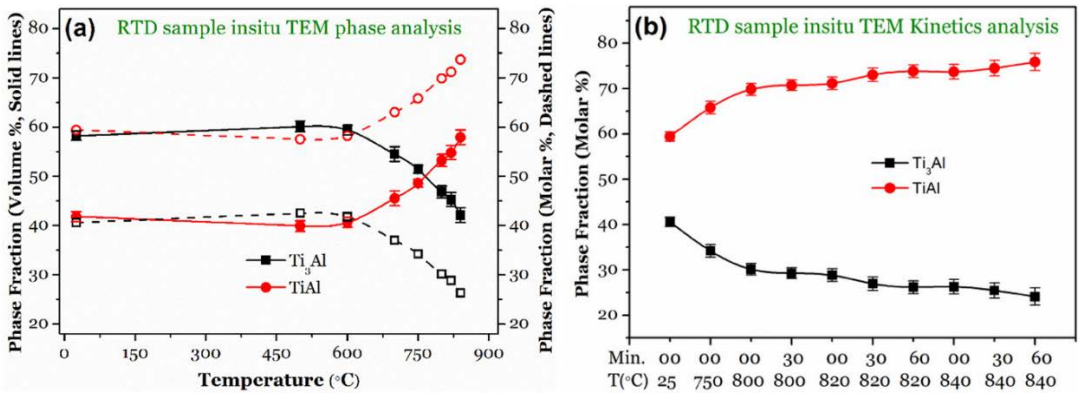

Figure 8

Open in figure viewerPowerPoint

(a) Phase fraction changes in RTD Ti48Al alloy with respect to temperature, and (b) phase fraction changes in RTD Ti48Al alloy with respect to temperature and time.

As per to the Ti-Al phase diagram, binary Ti-Al alloys should exhibit both α_2 and γ phases below 1300 °C and up to a maximum of 51 at% Al. Hence, Ti48Al should be a stable two-phase microstructure. Clemens and Mayer have described the occurrence of fully lamellar, nearly lamellar, or duplex microstructures depending on the actual composition and temperature.[13] Beyond 51% Al, the γ phase is stable, while the α_2 phase is stable between 28% and 38% Al.[42]

In both the RTD and NRTD samples, a nearly lamellar microstructure was observed at RT (Figure 3). From area EDS results, the overall composition of the NRTD sample at RT is 47.8 at% Al. At temperatures above 750 °C, a clear transition from the two-phase lamellar structure to a near gamma globular microstructure can be seen. This coincides with an increase in γ-TiAl phase content (Figure 8). In Figure 8b the phase content with respect to temperature and time is shown. From room temperature to 750 °C there is not much change in phase content. Starting from 800 °C (0 min) until 820 °C (60 min) there were significant changes in the content of the α_2-Ti_3Al and the γ-TiAl phases, with substantial changes taking place between 800 °C, 30 min to 820 °C, 60 min. For the 800 °C 30 min^{-1} condition, no significant change in the lamellar stability was observed. At 820 °C 10 min^{-1} the α_2-Ti_3Al phase fraction starts to fall by ≈2% and decreases on increasing the holding time until 60 min. The cumulative decrease in α_2-Ti_3Al is 11–12%. Based on the STEM-HAADF images for 840 °C, it can be stated that the structural integrity of the alloys is severely compromised, hence we have used 820 °C as the highest temperature in the subsequent analysis.

The deformed binary alloy maintains structural stability until it is significantly influenced by the combined effects of mechanical deformation and thermal energy. Introduction of cold work at room temperature provides interesting results when the alloy is subjected to high temperature exposure. Compared to samples without any room temperature deformation, it may be observed that the onset strain results in a wider temperature range (≈90 °C) for the complete destabilization of the lamellar structure in RTD samples. In the undeformed NRTD samples, the destabilization takes place at a fixed temperature and is dominated by quick spheroidization mechanism only as discussed above. Further, in both cases (RTD and NRTD), the temperature for complete instability is 840 °C.

To better understand the effect of strain on deformation, the interlamellar strain and strain of the α_2-Ti_3Al phase has been studied from the obtained TEM images using Strain++.[43] **Figure 9** shows the strain mapping of the NRTD samples in the x (ε_{xx}), xy shear force (ε_{xy}), and y (ε_{yy}) direction at RT, 750 and 820 °C respectively. With increasing T, the strain in the α_2-Ti_3Al phase marginally decreases from

2.2% (Figure 9a) in the RT sample to 2% (Figure 9b) for the 750 °C sample, drastically reducing to 0.9% in the 820 °C sample. This is consistent with the fast kinetics of NRTD samples presented in Figure 4. Moreover, strain in xx (ε_{xx}) and yy planes (ε_{yy}) are of the same magnitude, suggesting small texturing effect in these samples.

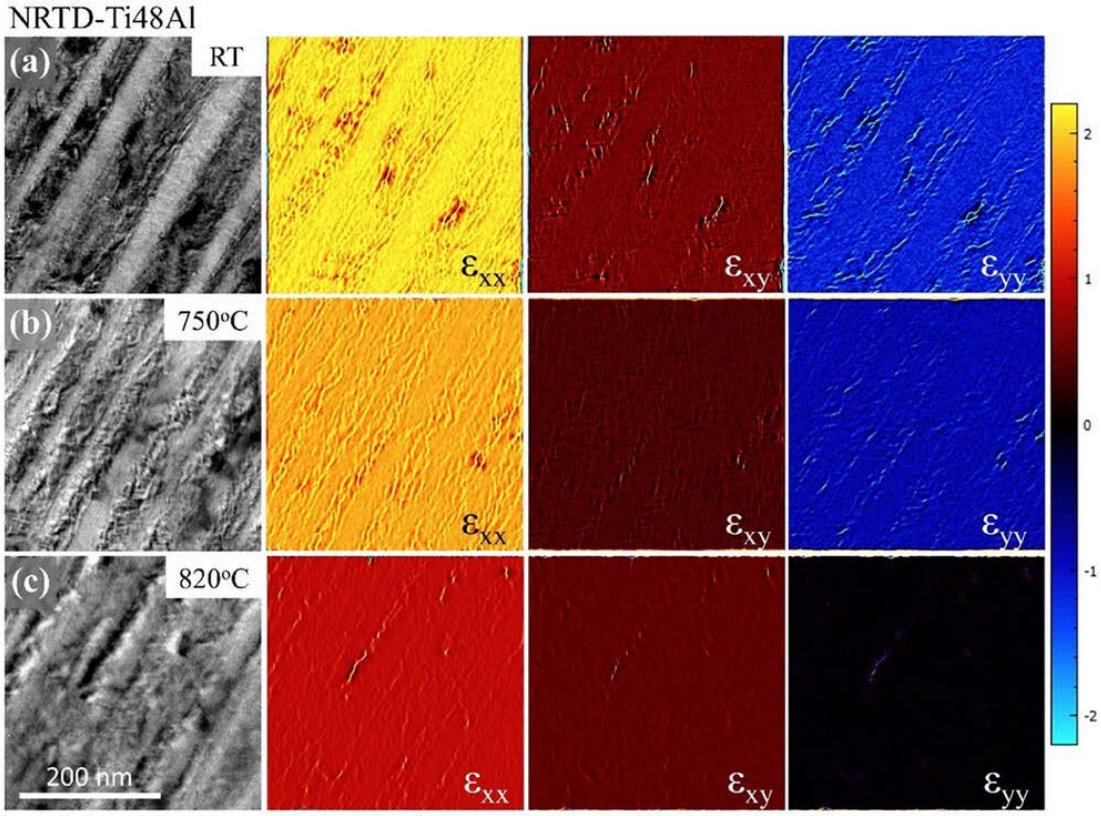

Figure 9

Open in figure viewerPowerPoint

Strain maps of the NRTD samples at (a) RT, (b) 750 °C, and (c) 820 °C.

The strain maps or the RTD sample are presented in **Figure 10** for the same temperatures and strain directions as prior. Overall, an increase in strain is observed between the NRTD and RTD samples as expected. This follows an increase in overall strain from 0.3% in the NRTD - RT sample to 0.8% in the RTD - RT sample as observed from XRD using the Williamson - Hall plot (Figure S3, Supporting Information). For this condition, the strain in the xx (ε_{xx}) plane is higher than that in xy planes (ε_{xy}) and yy planes (ε_{yy}), indicative of the texturing effect in the RTD samples. As the preferred orientation is in the <021> direction we observe more strain in the xx plane and less in yy plane.

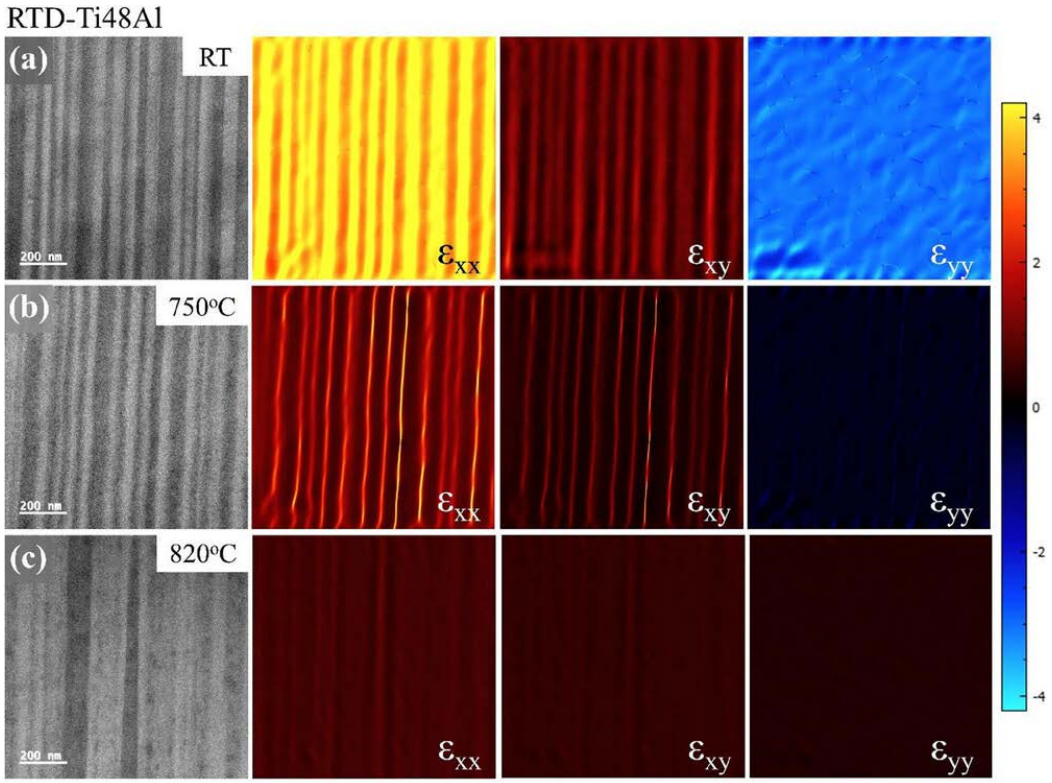

Figure 10

Open in figure viewerPowerPoint

Strain maps of the RTD samples at (a) RT, (b) 750 °C, and (c) 820 °C.

As the temperature is increased, the strain in the α_2-Ti_3Al phase decreases considerably, from 4.2% in the RT sample to 1.7% in the 750 °C sample to 1.2% in the 820 °C sample. This observation is consistent with the proposed mechanism of necking, breaking, and spherodization of α_2-Ti_3Al phase. It is observed that at high temperature in the RTD samples the initially well-defined α_2/γ interface becomes less defined and subsequently breaks down (becomes spheroidized) along with an increase in γ-TiAl phase fraction. The strain applied to the RTD-RT sample led to texturing and a decrease in interlamellar spacing, the increased defect density contributed to the instability of the lamellar structures. In the case of the NRTD samples, instability takes place quickly and is dominated by one single mechanism, i.e., spheroidization. The main models of lamellar instability at high temperature of cold worked samples include edge spheroidization, boundary splitting, termination migration and discontinuous coarsening.[44] Our in situ experimental studies clearly demonstrated that lamellar instability at high temperature is dominated by specific mechanisms depending upon the magnitude of the strain present in the sample.

In conclusion, introduction of cold work provides a gradual (parabolic) change in the initiation and progress of lamellar instability, while in the absence of cold work, the onset and completion of instability is rapid at a fixed temperature.

4 Conclusion

In situ Operando TEM studies were performed using the custom designed MEMS chip and Protochip TEM holder. In pre-strained samples, the instability mechanism starts with necking, followed by breakup of lamella and spheroidization spread over a temperature range of 750–820 °C. The instability of the lamellar structures was influenced by the presence of structural defects induced by deformation. During this process, the α_2-Ti_3Al phase fraction decreases by ≈12% while the γ-TiAl

phase fraction increases by the same amount. We found that the mechanically stored energy in the α_2 and the γ phases plays a crucial role in the lamellar instability in the Ti48Al alloy, resulting in a parabolic response of the instability mechanism spread over a temperature of 70 °C. On the other hand, samples without any room temperature deformation revealed lamellar instability at 820 °C, leading to quick spheroidization. Furnace annealed samples heat treated at 750 and 820 °C showed a similar trend as those of RTD and NRTD samples.

Acknowledgements

P.S.S.R.K. and J.V.V. contributed equally to this work and are co-first authors. The authors acknowledge financial support from Agency for Science, Technology and Research (A*STAR), Singapore under the Structural Metals and Alloys Program (Grant No.: A18B1b0061). This research is supported by the National Research Foundation, Singapore, under its 29th Competitive Research Programme (CRP) Call (Award ID NRF-CRP29-2022-0002). The authors acknowledge the Facilities for Analysis, Characterization, Testing, and Simulations (FACTS) at NTU for assistance and access to electron microscopy and X-Ray diffraction equipment. Xuesong Xu acknowledges the Jiangsu Funding Program for Excellent Postdoctoral Talent.

Conflict of Interest

The authors declare no conflict of interest.

References

- 1M. Thomas, M. P. Baco, *Aerospace Lab* 2011, 1.

Google Scholar

- 2P. V. Cobbinah, W. R. Matizamhuka, *Adv. Mater. Sci. Eng.* 2019, **2019**, 1.

View

Google Scholar

- 3H. Clemens, S. Mayer, *Mater. High. Temp.* 2016, **33**, 560.

View

CASWeb of Science®Google Scholar

- 4B. P. Bewlay, S. Nag, A. Suzuki, M. J. Weimer, *Mater. High. Temp.* 2016, **33**, 549.

View

CASWeb of Science®Google Scholar

- 5A. Knaislova, P. Novak, M. Cabibbo, L. Jaworska, D. Vojtech, *Materials* 2021, **14**, 1030.

View

CASPubMedGoogle Scholar

- 6M. Yamaguchi, H. Inui, K. Ito, *Acta Mater.* 2000, **48**, 307.

View

CASWeb of Science®Google Scholar

- 7B.-c. Lin, W. Chen, *China. Foundry.* 2021, **18**, 307.

View

Google Scholar

- 8X. Wu, *Intermetallics* 2006, **14**, 1114.

View

CASWeb of Science®Google Scholar

- 9M. Musi, B. Galy, J.-P. Monchoux, A. Couret, H. Clemens, S. Mayer, *Scr. Mater.* 2022, **206**, 114233.

View
CASWeb of Science®Google Scholar
- 10X. Liu, Q. Lin, W. Zhang, C. V. Horne, L. Cha, *Metals* 2021, **11**, 1644.
View
CASGoogle Scholar
- 11K. Kothari, R. Radhakrishnan, N. M. Wereley, *Progress. Aerospace. Sci.* 2012, **55**, 1.
View
Web of Science®Google Scholar
- 12V. Sharma, X. Tan, P. S. Sankara Rama Krishnan, S. Tekumalla, M. Duchamp, X. Xu, H. Ding, V. Chaudhary, R. V. Ramanujan, *Mater. Today. Commun*. 2023, **35**, 105831.
View
CASGoogle Scholar
- 13H. Clemens, S. Mayer, *Adv. Eng. Mater.* 2012, **15**, 191.
View
Google Scholar
- 14R. V. Ramanujan, *Int. Mater. Rev.* 2000, **45**, 217.
View
CASWeb of Science®Google Scholar
- 15R. V. Ramanujan, P. J. Maziasz, C. T. Liu, *Acta Mater.* 1996, **44**, 2611.
View
CASGoogle Scholar
- 16R. V. Ramanujan, *Acta Metall. Mater.* 1995, **32**, 4439.
View
Google Scholar
- 17R. V. Ramanujan, *Acta Metall. Mater.* 1994, **42**, 2775.
View
CASGoogle Scholar
- 18G. W. Qin, K. Oikawa, Z. M. Sun, S. Sumi, T. Ikeshoji, J. J. Wang, S. W. Guo, S. M. Hao, *Metall. Mater. Trans. A*. 2001, **32**, 1927.
View
Web of Science®Google Scholar
- 19D. S. Shong, Y.-W. Kim, *Scripta. Metallurgica*. 1989, **23**, 257.
View
CASGoogle Scholar
- 20J. D. Livingston, J. W. Cahn, *Acta Metall.* 1974, **22**, 495.
View
CASWeb of Science®Google Scholar
- 21H. Kimura, S. Kobayashi, O. Izumi, *Proc. Int. Symp. on Intermetallic CompoundsStructure and Mechanical Properties, JIMIS* 1991, **6**, 985.
Google Scholar
- 22P. J. Maziasz, R. V. Ramanujan, C. T. Liu, J. L. Wright, *Intermetallics* 1997, **5**, 83.
View
CASWeb of Science®Google Scholar
- 23M. Yamaguchi, H. Inui, S. Yokoshima, K. Kishida, D. R. Johnson, *Mater. Sci. Eng.,*

A. 1996, **213**, 25.
View
Google Scholar
- 24L. M. Hsiung, A. J. Schwartz, T. G. Nieh, *Intermetallics* 2004, **12**, 727.
View
CASGoogle Scholar
- 25X. Liu, L. Song, A. Stark, F. Pyczak, T. B. Zhang, *J. Mater. Sci. Technol*. 2023, **163**, 212.
View
CASGoogle Scholar
- 26S.-J. Youn, Y.-K. Kim, S.-W. Kim, K.-A. Lee, *Intermetallics* 2020, **124**, 106859.
View
CASWeb of Science®Google Scholar
- 27H. A. Soliman, M. Elbestawi, *Int. J. Adv. Manuf. Technol*. 2022, **119**, 5583.
View
Web of Science®Google Scholar
- 28L. F. Allard, W. C. Bigelow, M. Jose-Yacaman, D. P. Nackashi, J. Damiano, S. E. Mick, *Microsc. Res. Tech*. 2009, **72**, 208.
View
CASPubMedWeb of Science®Google Scholar
- 29S. Chu, P. Liu, Y. Zhang, X. Wang, S. Song, T. Zhu, Z. Zhang, X. Han, B. Sun, M. Chen, *Nat. Commun*. 2022, **13**, 4151.
View
CASPubMedWeb of Science®Google Scholar
- 30M. L. Taheri, E. A. Stach, I. Arslan, P. A. Crozier, B. C. Kabius, T. LaGrange, A. M. Minor, S. Takeda, M. Tanase, J. B. Wagner, R. Sharma, *Ultramicroscopy* 2016, **170**, 86.
View
CASPubMedWeb of Science®Google Scholar
- 31H. Zheng, Y. Zhu, *Ultramicroscopy* 2017, **180**, 188.
View
CASPubMedWeb of Science®Google Scholar
- 32X. Zhang, Y. Zhou, Y. Chen, M. Li, H. Yu, X. Li, *Sensors* 2023, **23**, 4470.
View
Google Scholar
- 33H. Zhang, R. Peng, J. Zhao, C. Fan, W. Feng, Z. Liu, *Nanomaterials* 2022, **12**, 4020.
View
CASPubMedGoogle Scholar
- 34E. Tyukalova, J. Vimal Vas, R. Ignatans, A. D. Mueller, R. Medwal, M. Imamura, H. Asada, Y. Fukuma, R. S. Rawat, V. Tileli, M. Duchamp, *Acc. Chem. Res*. 2021, **54**, 3125.
View
CASWeb of Science®Google Scholar
- 35H. Lee, O. F. N. Okello, G. Y. Kim, K. Song, S. Y. Choi, *Appl. Microsc*. 2021, **51**, 8.
View
PubMedGoogle Scholar
- 36M. Duchamp, Q. Xu, R. E. Dunin-Borkowski, *Microsc. Microanal*. 2014, **20**, 1638.

View
CASPubMedWeb of Science®Google Scholar
- 37P. W. Hawkes, J. C. H. Spence, *Springer Handbook of Microscopy*, Springer, Cham 2019.
View
Google Scholar
- 38C. Dwyer, *J. Phys.: Mater.* 2021, **4**, 042006.
View
CASGoogle Scholar
- 39S. J. Pennycook, P. D. Nellist, *Scanning Transmission Electron Microscopy-Imaging and Analysis*, Springer, New York 2011.
View
Google Scholar
- 40P. D. Nellist, S. J. Pennycook, *Adv. Imaging. Electron. Phys.* 2000, **113**, 147.
View
Web of Science®Google Scholar
- 41H. Husni, A. F. M. Noor, R. Astrawinata, *J. Eng. Technol. Sci.* 2013, **45**, 294.
View
Google Scholar
- 42V. Raghavan, *J. Phase. Equilibria. Diffusion.* 2005, **26**, 171.
View
CASWeb of Science®Google Scholar
- 43M. J. Hÿtch, E. Snoeck, R. Kilaas, *Ultramicroscopy* 1998, **74**, 131.
View
CASWeb of Science®Google Scholar
- 44G. Sharma, R. V. Ramanujan, G. P. Tiwari, *Acta Mater.* 2000, **48**, 875.
View
CASWeb of Science®Google Scholar